

RUBBER ENGINE INTEGRATED OPTIMIZATION STRATEGY FOR OVERALL AIRCRAFT DESIGN

Jannik Häßy[1], Jens Schmeink[1] & Benjamin Fröhler[2]

[1]Institute of Propulsion Technology, German Aerospace Center (DLR), Linder Höhe, 51147 Cologne, Germany
[2]Institute of System Architectures in Aeronautics, German Aerospace Center (DLR), Hein-Saß-Weg 22, 21129 Hamburg, Germany

Abstract

Aero-engines involve numerous design variables that strongly influence overall aircraft performance and objectives such as mission fuel burn, climate impact and costs. Evaluating many engine designs on aircraft level using detailed design workflows is computationally expensive. Then, optimization strategies that require many evaluations are impractical, e.g. design-of-experiment approaches and evolutionary or gradient-based optimization on top-level. This paper proposes a sub-level engine optimization strategy based on sensitivities of top-level objectives with respect to engine interface parameters, e.g. thrust specific fuel consumption, engine mass, nacelle dimensions and emissions. A low number of sensitivities is used to optimize the engine design with respect to top-level objectives before it is integrated and evaluated within the top-level aircraft design process. Start values for sensitivities are estimated according to the specific application throughout different workflow runs and can be refined with study calculation results. The proposed engine model integrated strategy is applied to a long-range, single-aisle aircraft with underwing engines using the top-level objectives mission fuel burn, operating empty mass and atmospheric temperature response to quantify climate impact. The results are benchmarked against a reference optimization strategy using a surrogate-based evolutionary optimization approach that requires a top-level design-of-experiment.

Keywords: Engine Design, Overall Aircraft Design, Optimization, Hybrid Surrogate-based Rubber Engine

1. Introduction

Multidisciplinary design analysis and optimization (MDAO) for aircraft has to resolve many interactions between different systems, components and disciplines. One important coupling is related to engine sizing and the selection of thermodynamic cycle parameters. Typically, workflows for overall aircraft design (OAD) integrate engine models to account for the impact of the discipline propulsion. The complexity and calculation effort for OAD workflows increases significantly with the level of detail of disciplinary models. When a single workflow execution is expensive in terms of calculation effort, the investigation of large design spaces or the use of optimizers on the top-level of the workflow becomes increasingly challenging. Figure 1 shows two different optimization strategies for the discipline propulsion within OAD, which are:

- **The DoE and Surrogate-based Optimization Strategy (Reference Approach):** Since the direct use of an optimizer on the top-level would be to expensive, the selected reference approach generates a sufficiently large design-of-experiment (DoE) and calculates all samples by converging the OAD workflow accounting for disciplinary iterations. The presented calculation efforts are taken from the demonstration study of a hybrid surrogate-based rubber engine model approach described in [1] similar to [2]. When the DoE is completed, surrogate models are trained to approximate the objectives, constraints and further parameters that are required

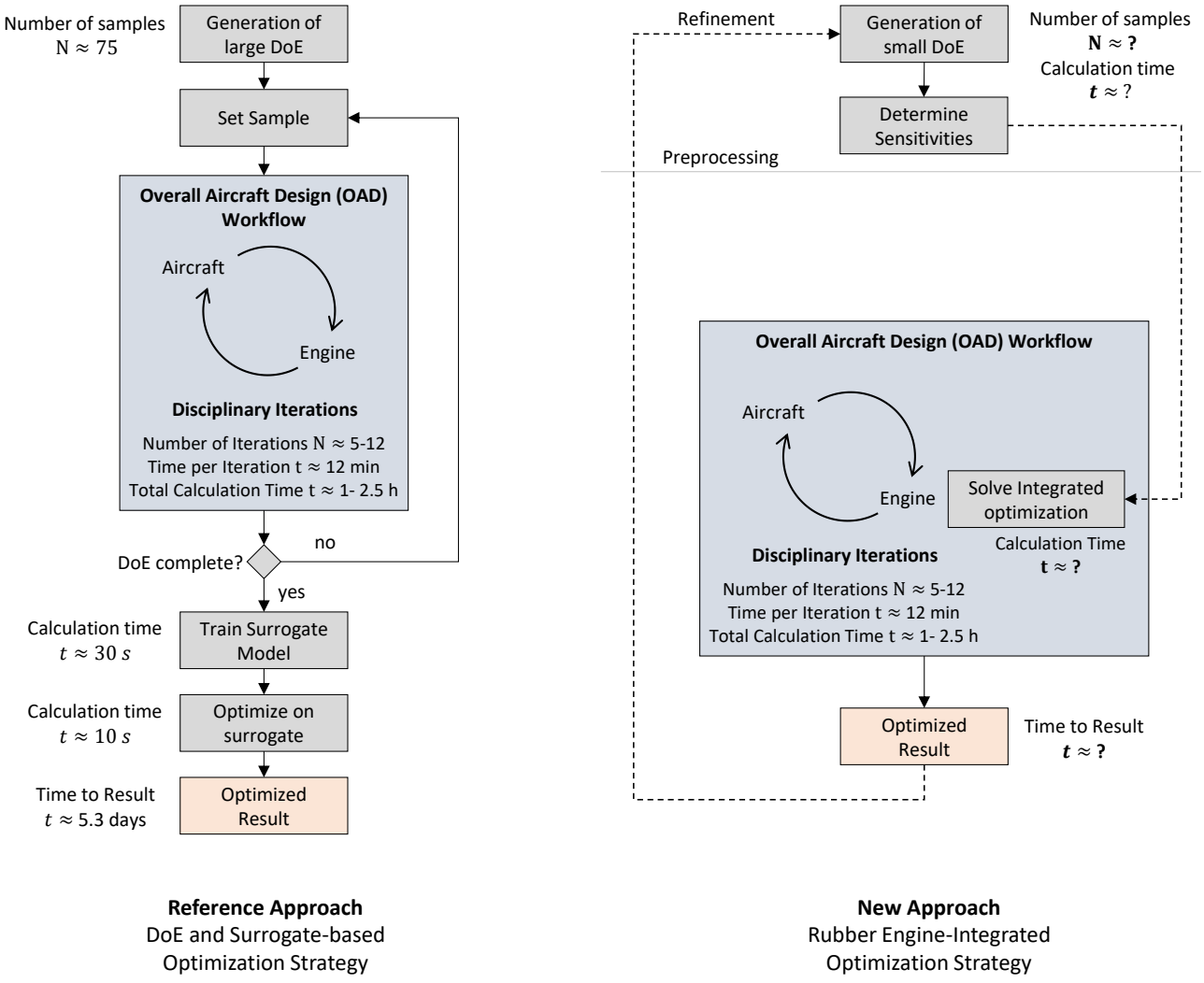


Figure 1 – Schematic of two different optimization strategies for the discipline propulsion within overall aircraft design: the reference approach using surrogate-based optimization (left) and the newly proposed engine model-integrated optimization strategy (right).

for the subsequent surrogate-based optimization. The effort for surrogate creation and the surrogate-based optimization are small compared to the execution of the OAD workflow and the generation of the training data. In total, a calculation time of 5.3 days is required to obtain a first optimized result. Employing adaptive sampling may reduce the required calculation time to a limited extend, but still many workflow executions are required, especially for multi-objective optimization problems where optimal solutions are distributed across a large parameter space.

- **Rubber Engine-Integrated Optimization Strategy (New Approach)**: To reduce the calculation time, a new approach is proposed that uses a rubber engine model-integrated optimization strategy. The engine is optimized already within the discipline propulsion itself for top-level objectives. The top-level objectives are approximated by means of a linear-superposition approach using constant sensitivities, which have to be determined in advance and are provided to the engine model. With this strategy, only one workflow run is required to obtain a first optimal result. However, additional effort is required to determine the sensitivities in a preprocessing step. With each resulting workflow output, the DoE for sensitivity estimation can be extended. It is unclear how many samples are required to obtain reliable sensitivities and whether the linearization approach is feasible for different common objectives such as mission fuel burn, overall system mass and climate impact.

This paper investigates the following research hypothesis:

Research Hypothesis

An engine model-integrated optimization strategy within overall aircraft design that is based on local sensitivities of top-level objectives with respect to engine interface parameters produces sufficiently similar optimization results with less computational effort compared to a top-level surrogate-based optimization approach that requires a large DoE.

2. Methodology

A conceptual design engine model is extended by implementing a sub-level optimization procedure based on sensitivities, i.e. local derivatives of top-level parameters with respect to engine model output parameters. The engine model is then integrated into an overall aircraft design workflow to solve a multi-objective engine optimization problem. The results are compared with the results solving the same problem by means of the reference surrogate-based optimization strategy. Both approaches are assessed with respect to the identified optimal engine designs and computational effort. The following sections present the physical models, problem definition and optimization approach.

2.1 Engine Model

The proposed optimization strategy can be used in combination with different types of engine models. Here, a hybrid surrogate-based rubber engine approach is employed according to [1, 2, 3] and as depicted in Fig. 2. The rubber engine model is created in a pre-processing step, separating engine design and engine selection. During the model creation phase, different engine designs are generated to populate a predefined design space using a certain sampling strategy. The multi-dimensional design space is spanned by the thrust requirements at sizing operating conditions and by engine design parameters. For this paper, a rubber engine model for an unmixed geared turbofan engine architecture with entry into service (EIS) in the year 2035 is used. The sizing thrusts are the corrected thrust at top-of-climb $\mathrm{FN}_{\mathrm{TOC}}$ and the thrust at maximum take-off $\mathrm{FN}_{\mathrm{MTO}}$, which is divided by $\mathrm{FN}_{\mathrm{TOC}}$ and prescribed as thrust ratio $\mathrm{FN}^{*}_{\mathrm{MTO/TOC}}$. The available engine design parameters comprise the bypass ratio at cruise conditions ($\mathrm{BPR}_{\mathrm{CR}}$), turbine inlet temperature at top-of-climb ($T_{41,\mathrm{TOC}}$) and maximum compressor outlet temperature ($T_{3,\mathrm{max}}$), which sets the overall pressure ratio. In the application phase, the rubber engine model enables the selection of a specific engine from the covered continuous design space for a given set of model input values according to equation 1.

$$\text{Engine Design} = f(\mathrm{BPR}_{\mathrm{CR}}, T_{41,\mathrm{TOC}}, T_{3,\mathrm{max}}, \mathrm{FN}_{\mathrm{TOC}}, \mathrm{FN}^{*}_{\mathrm{MTO/TOC}}) \tag{1}$$

The internal surrogate models (see Fig. 2) are then evaluated with the given input values. The predictions of the surrogate models are directly provided as output when they do not depend on the operating state of the engine, e.g. engine mass, dimensions, or are internally transferred to initialize an embedded tool for thermodynamic cycle analysis. With this embedded tool, the off-design performance of the selected engine design is calculated on-demand during application in OAD. The thermodynamic data is internally passed to an embedded model for emission calculation, which provides engine emissions corresponding to the engine performance data at the rubber engine model interface.

The creation of the rubber engine model is described in [1]. A conceptual engine design process similar to [2] is employed using the virtual propulsion framework *GTlab* (Gas Turbine Laboratory) [4, 5, 6]. The multidisciplinary design process combines a multi-point thermodynamic cycle analysis with a knowledge-based method for flow path sizing [7], a basic aerodynamic analysis of turbo machinery efficiencies [8], mass estimation on the level of single engine parts [7] and a model for the prediction of engine emissions [1, 2]. Applied in the OAD context, the rubberized engine enables the consideration of detailed interactions between the airframe and propulsion unit based on a sophisticated, expert-proven engine model.

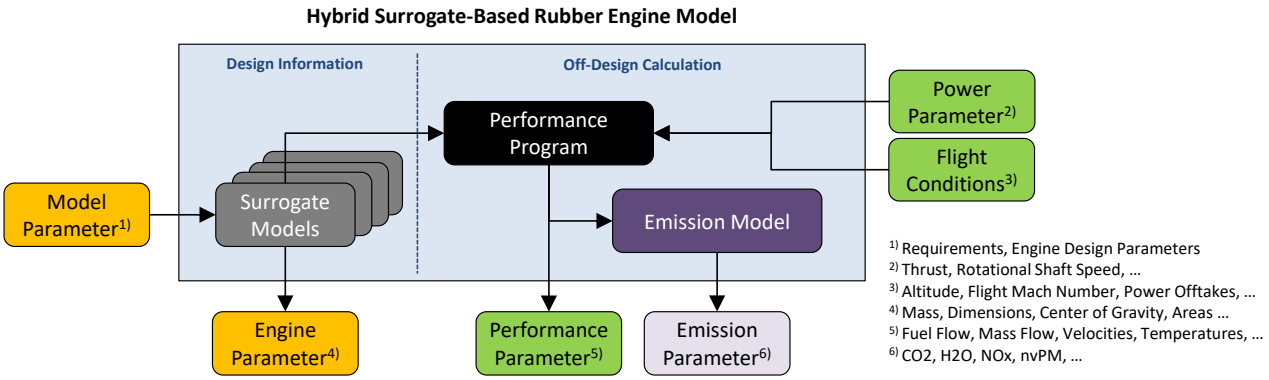


Figure 2 – Hybrid surrogate-based rubber engine model concept [2].

2.2 Aircraft Model

The long-haul, wide-body, generic aircraft model D300-XRF1 [9] is selected as reference aircraft. The D300-XRF1 is designed for 300 passengers with a 3-class cabin layout resulting in a fuselage with a length of 64 m. The ICAO aerodrome category E applies to the D300-XRF1 aircraft with a wingspan of 58 m and an aspect ratio of 9. By forecasting evolutionary technological improvements for the expected market maturity EIS = 2035, the reference aircraft is improved as described in [2]. In this publication, a modified version of the workflow presented by Fröhler et al. [9] is used as depicted in figure 3. The OAD workflow is implemented in the integration platform RCE (Remote Component Environment) [10] using the "Common Parametric Aircraft Configuration Schema" (CPACS), which provides a standardized format to support the communication between the different workflow components [11, 12].

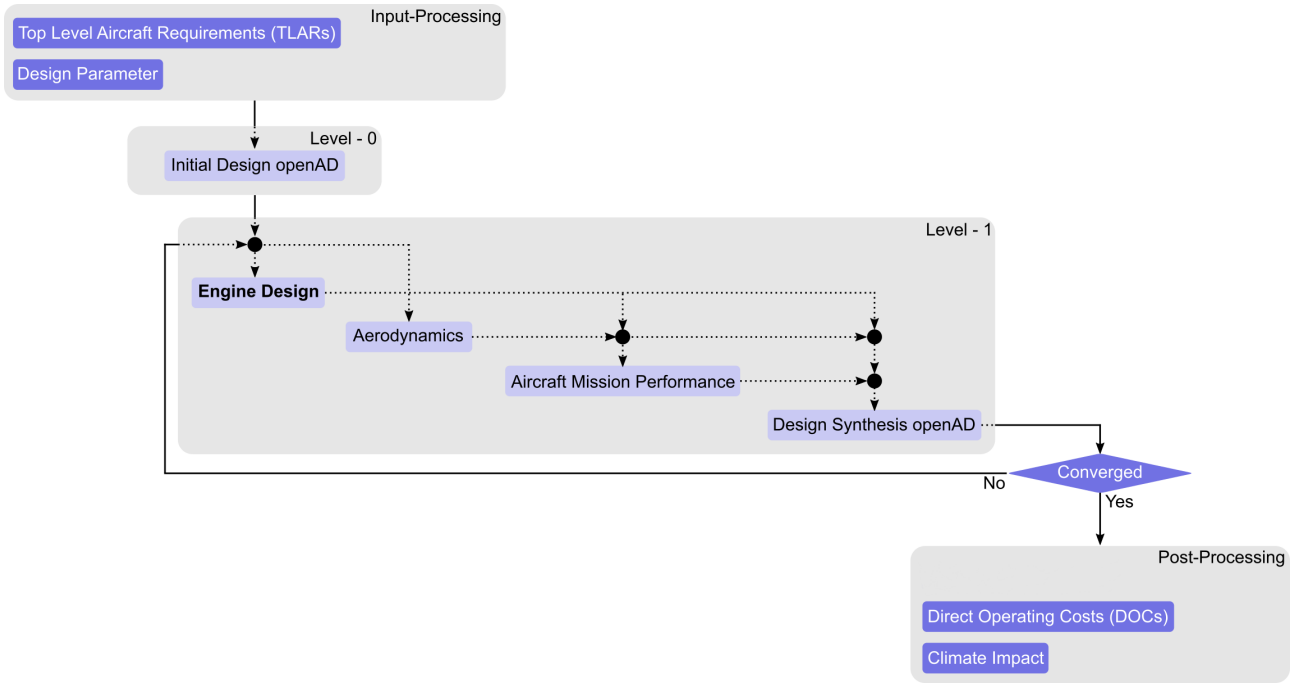


Figure 3 – Conceptual overall aircraft design process [2].

To initialize the OAD process, the level-0 conceptual design tool openAD [13] is used, which produces an initial geometry definition and an initial performance estimate of the aircraft based on the TLARs and design parameters. Subsequently, level-1 disciplinary tools with higher fidelity are integrated to refine the initial openAD results. In the engine design subprocess, the rubber engine model provides the engine properties and performance to other disciplinary models. As a final step, the higher fidelity results are fed back into openAD as a synthesis to obtain a consistent aircraft design. The level-1

is iterated until lift and drag coefficients at mid cruise conditions (CR), the maximum take-off mass and operating empty mass converge. The post-processing includes an assessment of the climate impact in terms of the metric average temperature response (ATR) according to [14] assuming an operational lifetime of 30 years, a maximum integration window of 100 years (ATR = ATR_{100}) and disabling discount weighting using a devaluation rate of zero.

2.3 Engine Optimization Problem

An exemplary study is performed to demonstrate the proposed engine model-integrated optimization strategy for OAD and to benchmark the approach against the reference optimization procedure (see Fig. 1). Therefore, the optimization problem in equation 2 is formulated according to [1]. The different objectives mission fuel burn (FB), average temperature response (ATR) and operating empty mass (OEM) lead to a three-dimensional Pareto-front. To choose a single design from the Pareto-front, specified weights $\mathbf{w}$ are used to compile a scalar objective function. The decision variables are the engine parameters BPR, $T_{41,\mathrm{TOC}}$ and $T_{3,\max}$ for which upper and lower bounds are defined. The optimization is additionally subject to different constraints $\mathbf{g}(\mathbf{x})$ and $\mathbf{h}(\mathbf{x})$ to ensure feasible engine designs accounting for maximum temperatures, minimum blade dimensions, minimum surge margins, maximum stage count (see Tab. 1).

$$\min_{\mathbf{x}\in\mathbb{R}^3} \mathbf{f}(\mathbf{x}) = \begin{bmatrix} \mathrm{FB}(\mathbf{x})/\mathrm{FB}_{\mathrm{ref}} \\ \mathrm{ATR}(\mathbf{x})/\mathrm{ATR}_{\mathrm{ref}} \\ \mathrm{OEM}(\mathbf{x})/\mathrm{OEM}_{\mathrm{ref}} \end{bmatrix} \cdot \begin{bmatrix} w_1 \\ w_2 \\ w_3 \end{bmatrix} \quad \text{with} \quad \mathbf{x} = \begin{bmatrix} \mathrm{BPR} \\ T_{3,\max} \\ T_{41,\mathrm{TOC}} \end{bmatrix}, \quad \sum_{i=1}^{3} w_i = 1 \quad \text{and} \quad 0 \le w_i \le 1$$

$$\text{s.t. } \mathbf{x}_{\mathrm{lb}} \le \mathbf{x} \le \mathbf{x}_{\mathrm{ub}}, \quad \mathbf{g}(\mathbf{x}) \le \mathbf{0}, \quad \mathbf{h}(\mathbf{x}) \ge \mathbf{0} \tag{2}$$

$$\text{where} \quad \mathbf{x}_{\mathrm{lb}} = \begin{bmatrix} 10 \\ 850 \\ 1700 \end{bmatrix} \quad \text{and} \quad \mathbf{x}_{\mathrm{ub}} = \begin{bmatrix} 16 \\ 1000 \\ 1760 \end{bmatrix}$$

Table 1 – Constraints for engine selection during the exemplary optimization study from [1].

Parameter	Symbol	Unit	Value	type
Compressor Outlet Temperature	$T_{3,\max}$	[K]	≤ 1000	$g(x)$
HPC Outlet Blade Height	$h_{\mathrm{HPC,out}}$	[mm]	≥ 12	$h(x)$
HPT 1St. NGV Outlet Temperature at TOC	$T_{41,\mathrm{TOC}}$	[K]	≤ 1750	$g(x)$
HPT 1St. NGV Outlet Temperature at Cruise	$T_{41,\mathrm{CR}}$	[K]	≤ 1600	$g(x)$
HPT 1St. NGV Outlet Temperature MAX	$T_{41,\max}$	[K]	≤ 2000	$g(x)$
LPT Entry Temperature	$T_{45,\max}$	[K]	≤ 1275	$g(x)$
Fan Tip Radius	$R_{\mathrm{t,Fan}}$	[m]	≤ 1.7	$g(x)$
HPC Stage Count	N_{HPC}	[-]	≤ 10	$g(x)$
LPT Stage Count	N_{LPT}	[-]	≤ 4	$g(x)$
Fan Surge Margin	$\mathrm{SM}_{\mathrm{Fan}}$	[%-points]	≥ 3.25	$h(x)$

2.4 Optimization Strategy

The optimization problem formulated in equation 2 can only be solved on the top-level since the objectives are results of complete workflow runs. However, the optimization problem can be reformulated to yield an approximate variant that is solvable on engine level (see Eq. 3).

$$\min_{\mathbf{x}\in\mathbb{R}^3} \mathbf{f}(\mathbf{x}) = \sum_{j=1}^{m} w_j \left(1 + \Delta M_j\right) \quad \text{with} \quad \Delta M_j = \frac{M_j - M_{j,\mathrm{ref}}}{M_{j,\mathrm{ref}}} = \sum_{i=1}^{n} \frac{\partial M_j}{\partial p_i} \frac{p_i(\mathbf{x}) - p_{i,\mathrm{ref}}}{p_{i,\mathrm{ref}}} \tag{3}$$

The sensitivities $\partial M_j / \partial p_i$ describe the local, partial derivatives of the objectives M_j with respect to the engine parameters p_i. The objectives are FB, ATR and OEM. The engine parameters are e.g. the thrust specific energy consumption (TSFC), bare engine mass (M), maximum nacelle diameter (D),

nacelle length (L) or emission index for nitrogen oxides (EINOx). Both, the objective values and the engine parameters are expressed as relative changes with respect to constant reference values $M_{j,\mathrm{ref}}$ and $p_{i,\mathrm{ref}}$. With this formulation, a linear relation between the objective M_j and the relative change in the parameter p_i is assumed. Please note that the relative change in p_i can still contribute with a non-linear characteristic. Different single effects (n) are superimposed to estimate the total change in the objective. It is important, that all relevant coupling effects between engine parameters and the objective are captured to obtain reliable relative changes of the objective ΔM_j.
The sensitivity values have to be representative for the investigated application case and the specific workflow setup. One option to calculate the sensitivities is by means of linear least-squares regression using a sampling with N_S different designs, which are the converged results of OAD workflow executions. Each additional workflow execution can later be used to refine the sampling and to update the coefficients (see Fig. 1).
The normalized response of an objective M_j is approximated with equation 4 where $c_{ji} = \partial M_j / \partial p_i$ denotes the sensitivity coefficient of objective M_j with respect to engine interface parameter p_i.

$$\Delta M_j = \frac{M_j - M_{j,\mathrm{ref}}}{M_{j,\mathrm{ref}}} \approx \sum_{i=1}^{n} c_{ji} \frac{\Delta p_i}{p_{i,\mathrm{ref}}}, \tag{4}$$

The resulting coefficients provide an estimate of the local sensitivities and quantify the influence of each engine parameter on the considered objective. The root mean squared error (RMSE) in equation 5 is applied to determine the quality of the regression where y_k and $\hat{y}_k$ denote the observed and predicted relative objective changes, respectively.

$$\mathrm{RMSE} = \sqrt{\frac{1}{N_\mathrm{S}} \sum_{k=1}^{N_\mathrm{S}} (y_k - \hat{y}_k)^2} \tag{5}$$

Furthermore, the rank and singular values of the regression matrix are evaluated to identify potential collinearity among the engine parameters and to ensure a numerically stable estimation of the sensitivity coefficients.

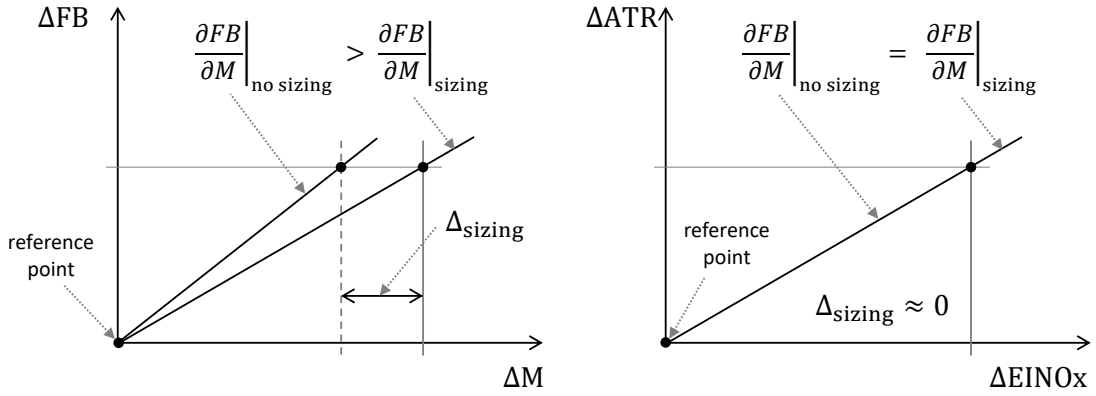


Figure 4 – Schematic of sensitivities and the influence of engine resizing.

Figure 4 schematically visualizes the sensitivity definition for $\partial \mathrm{FB}/\partial M$ and $\partial \mathrm{ATR}/\partial \mathrm{EINOx}$ considering only two points: The reference sample and one other sample. For each parameter, the Δ-value to its reference is estimated and plotted. Then, the gradient of the linear function is the sensitivity coefficient. To ensure that the coefficient value is used properly, it is important to specify whether the sensitivity includes effects due to engine resizing. For example, when the engine design changes and its mass increases, this increase is amplified at the aircraft level: A higher engine mass leads to a higher overall aircraft mass, which results in a higher required thrust. When the engine is resized to fulfil the higher thrust requirement, the engine size and mass increases. When the sensitivity was calculated including this amplification in ΔM, the resizing effect must also be accounted for when the sensitivity is applied to approximate the change in the objective FB. Parameters that are subject to engine resizing effects are e.g. engine mass, diameter and length. Other parameters

that mainly depend on thermodynamic cycle parameters are approximately invariant with respect to such engine resizing effects, e.g. the TSFC, which relates the fuel flow to the generated thrust, or emission index EINOx, which relates the mass of emitted nitrogen oxides to the mass of fuel burned. However, thermodynamic parameters are influenced by thrust ratios and the engine's thrust lapse characteristic. For example, when the ratio of required thrusts at cruise or take-off relative to top-of-climb change, this relative change is reflected in thermodynamic parameters. If $\mathrm{FN}_{\mathrm{TOC}}$ remains the same but $\mathrm{FN}_{\mathrm{CR}}$ increases, the throttle setting and operating temperatures of the engine will change at CR relative to TOC, e.g. having an effect on NOx. Therefore, additional sensitivities are introduced to map how the thrust demand will change with engine parameters similar to the change of objectives in equation 3.
In order to solve the approximated optimization problem from equation 3, an optimizer is integrated into the rubber engine model concept depicted in figure 2. Figure 5 presents the implemented engine model-integrated optimization process. The following steps are necessary:

1. The required thrusts at CR, TOC and MTO are provided from OAD at the interface to the hybrid surrogate-based rubber engine model.

2. The rubber engine model is evaluated for the currently selected input parameters according to equation 1 and the performance of the selected engine is calculated for cruise operation.

3. Based on the engine parameters of the currently selected engine, the change in required thrust is determined using the approximation based on sensitivities. The difference between the previously set model input and the approximated required thrust is $\Delta\mathrm{FN}$.

4. As long as $\Delta\mathrm{FN}$ is higher than a certain tolerance value, the thrust input for the rubber engine model evaluation is iteratively updated until convergence is reached.

5. The changes in objectives are evaluated using the approximation based on the superposition approach with constant sensitivities assuming linear relations between ΔM_j and Δp_i.

6. The constraints are evaluated for the currently selected engine design.

7. The optimizer varies the decision parameters $\mathrm{BPR}_{\mathrm{CR}}$, $T_{41,\mathrm{TOC}}$ and $T_{3,\max}$ to optimize the weighted scaler objective. For each optimizer iteration, the steps (2), (3) and (4) are repeated until the approximated required thrust is converged.

8. When the optimizer found the solution, the rubber engine model is evaluated once more with the optimal values for decision variables and the initially requested thrust from step (1).

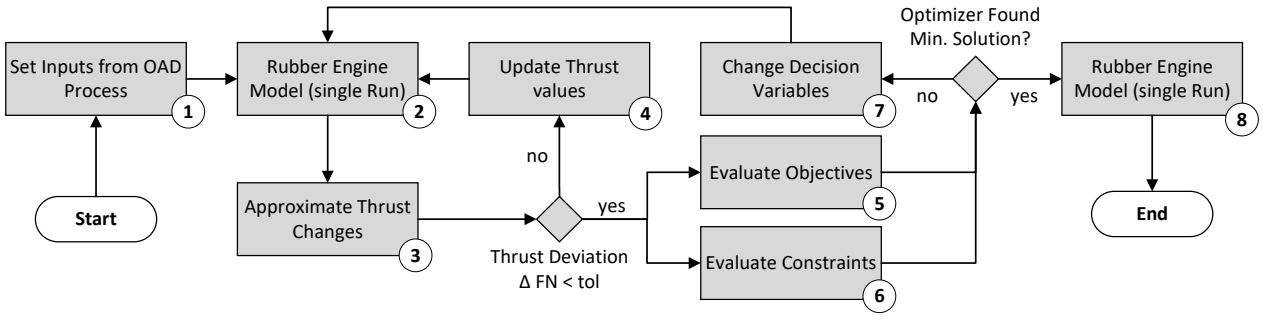


Figure 5 – Overview of the rubber engine-integrated optimization process.

The optimization is carried out using the NLopt library [15] and the derivative-free COBYLA (Constrained Optimization BY Linear Approximations) algorithm [16]. COBYLA is particularly well suited for simulation-based engineering optimization problems since it does not require analytical gradients of the objective or constraint functions. Instead, the algorithm constructs local linear approximations of the objective and constraint functions and iteratively updates the design variables while maintaining

feasibility with respect to nonlinear constraints. This makes COBYLA a robust choice for problems involving black-box models and multiple nonlinear constraints. To improve numerical conditioning and convergence, all design variables and constraint values were normalized prior to optimization. Relative stopping tolerances are specified for both the objective function and the decision variables, while a constraint tolerance is applied to all inequality constraints. Design variables are constrained by the prescribed lower and upper bounds and the optimization is initialized at the midpoint of the normalized design space.

3. Results

Figure 6 shows the two-dimensional FB-ATR-projection of the Pareto-front that is obtained by solving the optimization problem by means of the reference strategy as presented in [1]. A DoE with 75 samples (number of required top-level workflow runs) was generated and the workflow converged for 71 samples. A radial basis function (RBF) surrogate model with a cubic kernel and regression was fitted to the data using the software *SMARTy* [17]. Then, the population-based evolutionary algorithm NSGA-III from the python library *pymoo* [18] was used to solve the multi-objective optimization problem (see Eq. 2). The resulting Pareto-front shows a trade-off between FB, ATR and OEM (see Fig. 6) and a detailed physical analysis of the results is presented in [1]. Engine designs were selected by applying different weighting coefficients $\mathbf{w}$. In a first step, different weighted-best lines are estimated for different weights of OEM w_{OEM}. Then different engine designs are selected on the Pareto-line for $w_{\mathrm{OEM}} = 0.1$. The min. FB design ($w_{\mathrm{FB}} = 0.9$, $w_{\mathrm{ATR}} = 0$, $w_{\mathrm{OEM}} = 0.1$), the min. ATR design ($w_{\mathrm{FB}} = 0.0$, $w_{\mathrm{ATR}} = 0.9$, $w_{\mathrm{OEM}} = 0.1$) and as a compromise a balanced design ($w_{\mathrm{FB}} = 0.7$, $w_{\mathrm{ATR}} = 0.2$, $w_{\mathrm{OEM}} = 0.1$), which allows small penalties in FB to reduce ATR, i.e. climate impact. The weighted-best line with $w_{\mathrm{OEM}} = 0.1$ and the three selected designs are used in this paper as reference case to compare the results of the newly proposed engine model-integrated optimization strategy with.

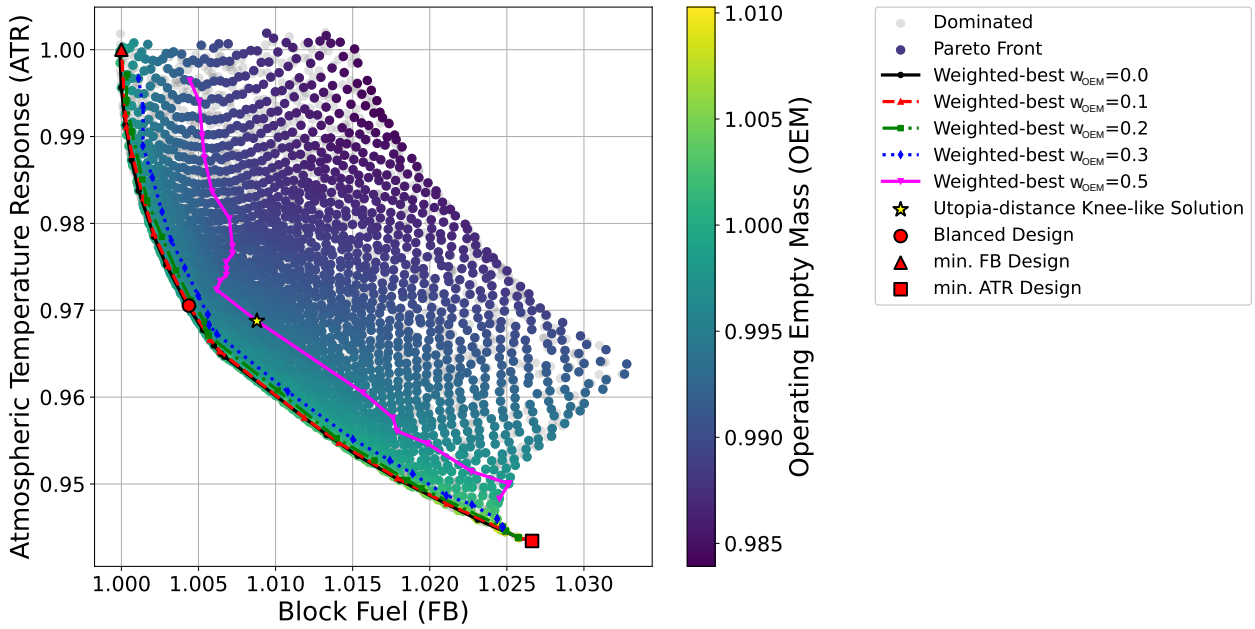


Figure 6 – Reference solution for the multi-objective optimization problem from equation 2 before the weights are applied showing the two-dimensional FB-ATR-projection of the Pareto-front from [1]. Different engine designs are selected by applying the different sets of weighting coefficients.

3.1 Sensitivity Results

The available samples $N_{\mathrm{S}} = 71$ of the reference case are used to investigate and determine sensitivities for the aircraft-engine coupling within the used OAD workflow. For each objective or thrust parameter, different engine parameters are tested for their influence and a set of parameters is identified that leads to a close approximation. The resulting dependencies are presented in the subsequent

equations (see Eq. 6 to 11), the determined sensitivity coefficients are provided in table 2 and the quality of approximation is shown in figure 8 comparing the sensitivity-based approximation with the sampled workflow results, which are referred to as 'Reference'.
For the mission fuel burn, dependencies on TSFC, engine mass, nacelle diameter and nacelle length are found as formulated in equation 6. These dependencies are typically used in conceptual engine design in order to estimate changes with respect to FB. Based on the findings in this paper, it is recommended to use the diameter and length of the nacelle instead of the nacelle wetted area or drag counts. First, the nacelle diameter might be sizing for the landing gear length and second, length and diameter typically have different impacts on nacelle drag, which cannot be captured just by the wetted area. Figure 7a shows that the approximation has a high quality: The change in FB over the investigated parameter space is of the order 9 % and the relative prediction errors are significantly below $\pm$ 0.5 %.

$$\Delta\mathrm{FB} = \frac{\partial \mathrm{FB}}{\partial \mathrm{TSFC}} \frac{\mathrm{TSFC} - \mathrm{TSFC_{ref}}}{\mathrm{TSFC_{ref}}} + \frac{\partial \mathrm{FB}}{\partial \mathrm{M}} \frac{\mathrm{M} - \mathrm{M_{ref}}}{\mathrm{M_{ref}}} + \frac{\partial \mathrm{FB}}{\partial \mathrm{D}} \frac{\mathrm{D} - \mathrm{D_{ref}}}{\mathrm{D_{ref}}} + \frac{\partial \mathrm{FB}}{\partial \mathrm{L}} \frac{\mathrm{L} - \mathrm{L_{ref}}}{\mathrm{L_{ref}}} \tag{6}$$

In the case of OEM, the same parameter dependencies are found according to equation 7 also having a high quality of approximation with prediction errors significantly less than $\pm$ 0.5 %-points as shown is figure 7b.

$$\Delta\mathrm{OEM} = \frac{\partial \mathrm{OEM}}{\partial \mathrm{TSFC}} \frac{\mathrm{TSFC} - \mathrm{TSFC_{ref}}}{\mathrm{TSFC_{ref}}} + \frac{\partial \mathrm{OEM}}{\partial \mathrm{M}} \frac{\mathrm{M} - \mathrm{M_{ref}}}{\mathrm{M_{ref}}} + \frac{\partial \mathrm{OEM}}{\partial \mathrm{D}} \frac{\mathrm{D} - \mathrm{D_{ref}}}{\mathrm{D_{ref}}} + \frac{\partial \mathrm{OEM}}{\partial \mathrm{L}} \frac{\mathrm{L} - \mathrm{L_{ref}}}{\mathrm{L_{ref}}} \tag{7}$$

Equation 8 shows the parameter dependencies for ATR. The climate impact of emitted CO_2, H_2O and NOx depend on the absolute amount of fuel burned and therefore, on the change in fuel burn ΔFB. Additionally, the emitted mass of NOx also depends on the emission index EINOx, which changes with the thermodynamic parameters of the engine. This is accounted for with the sensitivity $\partial\mathrm{ATR}/\partial\mathrm{EINOx}$. The impact of contrails and aircraft induced cloudiness (AiC) depends on the flight altitude, which is considered by the relative change in flight altitude at TOC. Please note that the effect of AiC can only be linearized over a narrow range of altitudes (cf. [14]). The approximation of relative changes in ATR is presented in 7c and has a moderate prediction error of ± 0.5 %-points.

$$\Delta\mathrm{ATR} = \frac{\partial \mathrm{ATR}}{\partial \mathrm{FB}} \Delta\mathrm{FB} + \frac{\partial \mathrm{ATR}}{\partial \mathrm{EINOx}} \frac{\mathrm{EINOx} - \mathrm{EINOx_{ref}}}{\mathrm{EINOx_{ref}}} + \frac{\partial \mathrm{ATR}}{\partial \mathrm{H_{TOC}}} \frac{\mathrm{H_{TOC}} - \mathrm{H_{TOC,ref}}}{\mathrm{H_{TOC,ref}}} \tag{8}$$

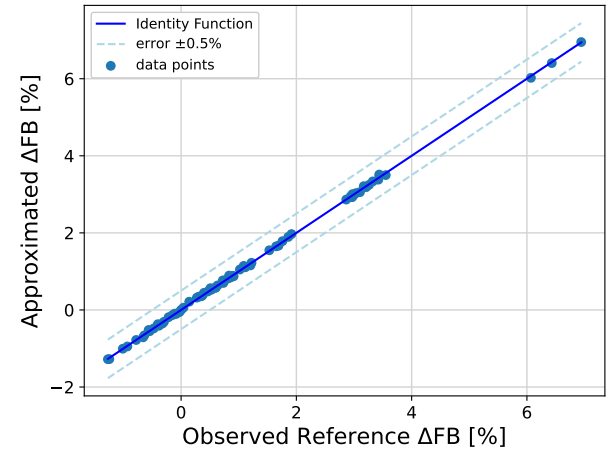
The change in the corrected thrust at TOC $\Delta\mathrm{FN}_{TOC}$ and the thrust ratio $\Delta\mathrm{FN}^*_{CR/TOC}$ are approximated in dependence on TSFC, M, D and L, in the same way as for FB and OEM (see equations 9 and 10). Figures 7d and 7e show that prediction errors are less than ± 0.5 %-points.

$$\Delta\mathrm{FN_{TOC}} = \frac{\partial \mathrm{FN_{TOC}}}{\partial \mathrm{TSFC}} \frac{\mathrm{TSFC} - \mathrm{TSFC_{ref}}}{\mathrm{TSFC_{ref}}} + \frac{\partial \mathrm{FN_{TOC}}}{\partial \mathrm{M}} \frac{\mathrm{M} - \mathrm{M_{ref}}}{\mathrm{M_{ref}}} + \frac{\partial \mathrm{FN_{TOC}}}{\partial \mathrm{D}} \frac{\mathrm{D} - \mathrm{D_{ref}}}{\mathrm{D_{ref}}} + \frac{\partial \mathrm{FN_{TOC}}}{\partial \mathrm{L}} \frac{\mathrm{L} - \mathrm{L_{ref}}}{\mathrm{L_{ref}}} \tag{9}$$

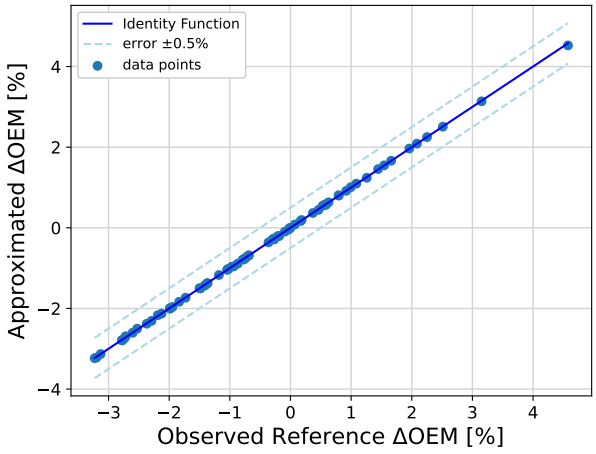
$$\Delta\mathrm{FN^*_{CR}} = \frac{\partial \mathrm{FN^*_{CR}}}{\partial \mathrm{TSFC}} \frac{\mathrm{TSFC} - \mathrm{TSFC_{ref}}}{\mathrm{TSFC_{ref}}} + \frac{\partial \mathrm{FN^*_{CR}}}{\partial \mathrm{M}} \frac{\mathrm{M} - \mathrm{M_{ref}}}{\mathrm{M_{ref}}} + \frac{\partial \mathrm{FN^*_{CR}}}{\partial \mathrm{D}} \frac{\mathrm{D} - \mathrm{D_{ref}}}{\mathrm{D_{ref}}} + \frac{\partial \mathrm{FN^*_{CR}}}{\partial \mathrm{L}} \frac{\mathrm{L} - \mathrm{L_{ref}}}{\mathrm{L_{ref}}} \tag{10}$$

The change of required thrust at maximum take-off $\Delta\mathrm{FN_{MTO}}$ is approximated based on the parameters TSFC and nacelle diameter only since no clear influence of other parameters was found (see Eq. 11). The quality of the approximation is lower compared to the other thrust parameters as shown in figure 7f with prediction errors significantly higher than ± 0.5 %-points. The take-off process is a complex interplay of various aircraft-level parameters and requirements, which are not available on engine level but that influence the required take-off thrust. Therefore, a moderate to high uncertainty has to be expected with respect to MTO. However, the general qualitative trend is captured by the approximation model.

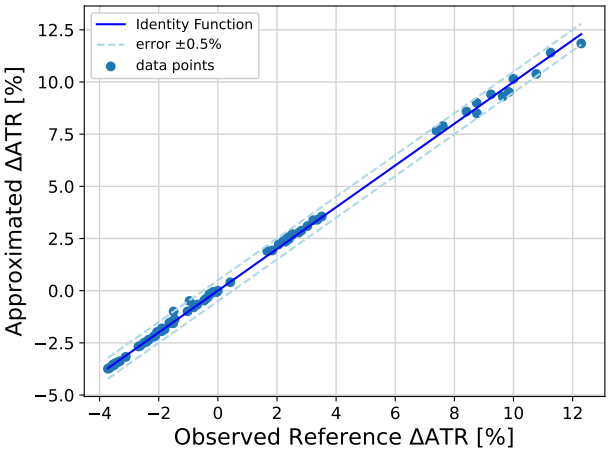
$$\Delta\mathrm{FN_{MTO}} = \frac{\partial \mathrm{FN_{MTO}}}{\partial \mathrm{TSFC}} \frac{\mathrm{TSFC} - \mathrm{TSFC_{ref}}}{\mathrm{TSFC_{ref}}} + \frac{\partial \mathrm{FN_{MTO}}}{\partial \mathrm{D}} \frac{\mathrm{D} - \mathrm{D_{ref}}}{\mathrm{D_{ref}}} \tag{11}$$



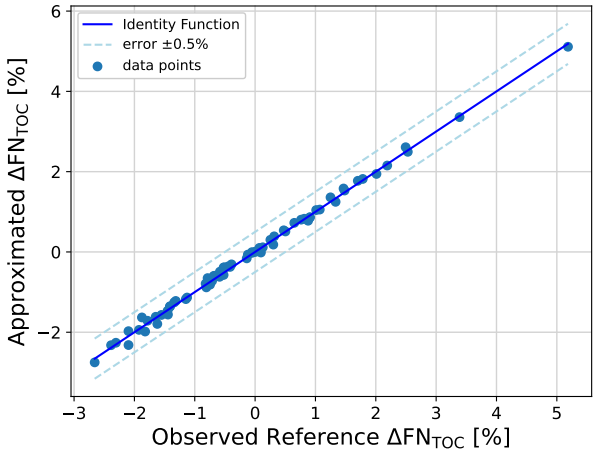
(a) Fuel Burn ΔFB



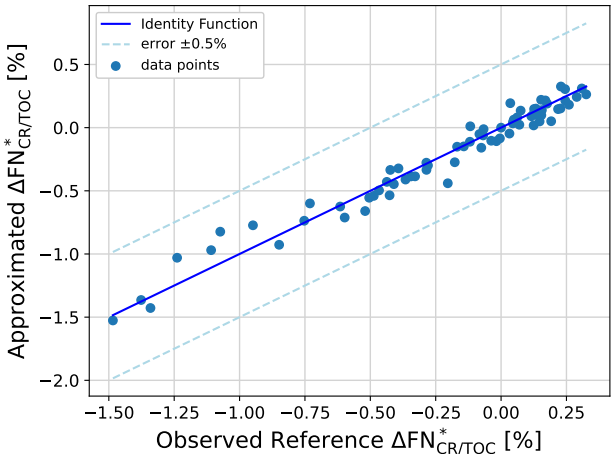
(b) Operating Empty Mass ΔOEM



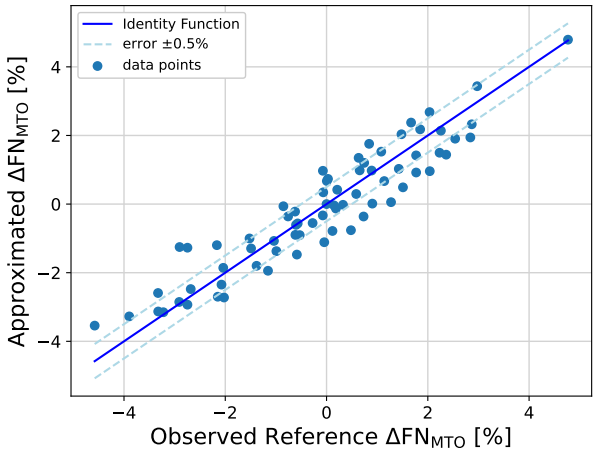
(c) Average Temperature Response ΔATR



(d) Corrected Thrust at top-of-climb ΔFN_{TOC}

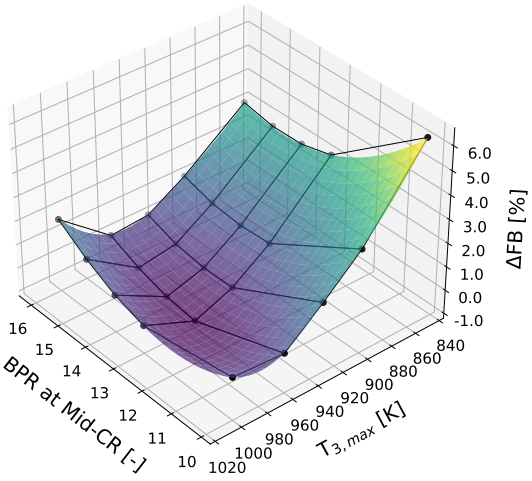


(e) Thrust Ratio $\Delta FN^*_{CR/TOC}$

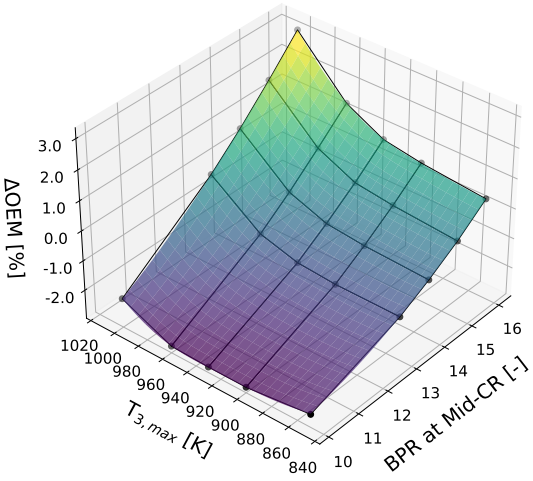


(f) Thrust at max. take-off ΔFN_{MTO}

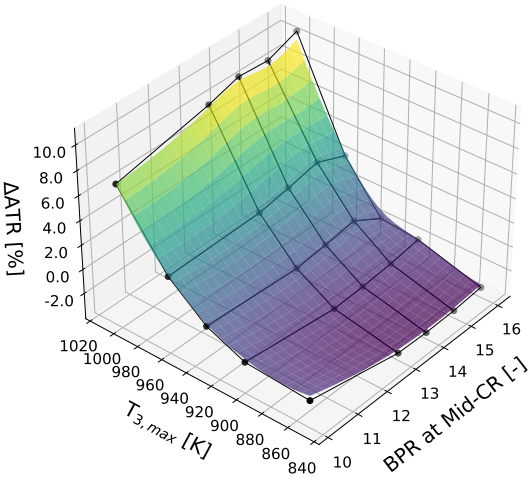
Figure 7 – Comparison between the sensitivity-based approximation and the observed reference values from the workflow result sampling for the objectives and thrust parameters. A prediction error of $\pm$ 0.5 %-points is shown to judge on the quality of approximation.



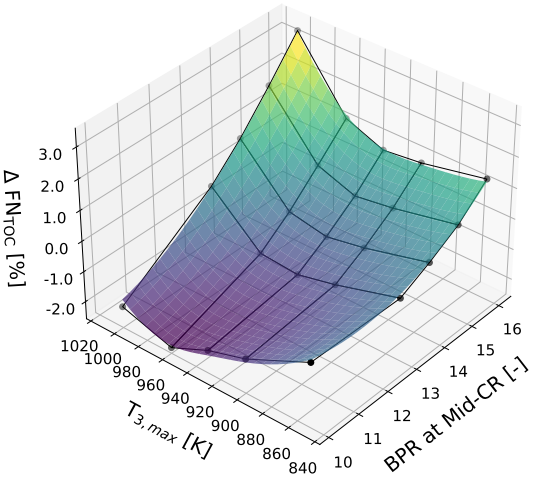
(a) Mission Fuel Burn ΔFB



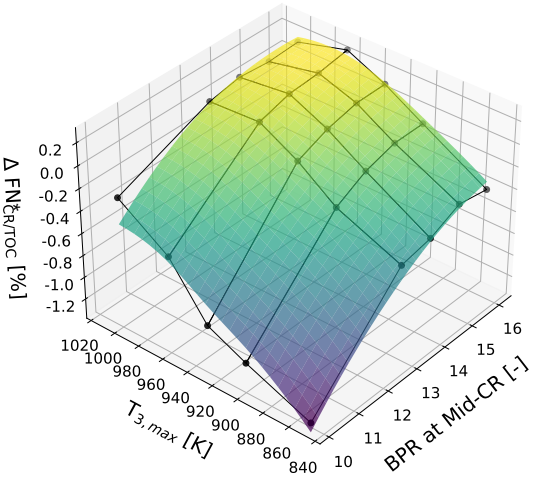
(b) Operating Empty Mass ΔOEM



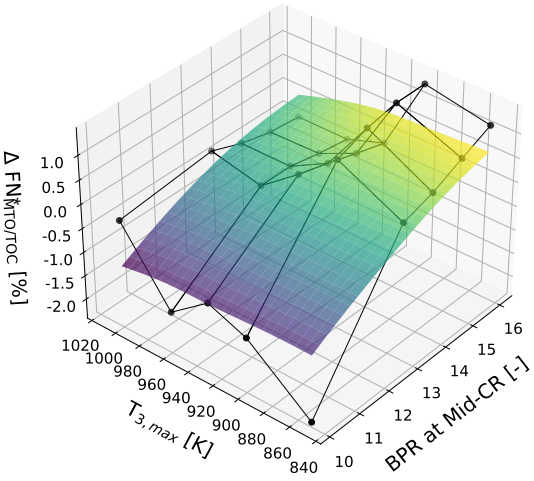
(c) Average Temperature Response ΔATR



(d) Corrected Thrust ΔFN_{TOC}



(e) Thrust Ratio CR to TOC $\Delta FN^*_{CR/TOC}$



(f) Thrust Ratio MTO to TOC $\Delta FN^*_{MTO/TOC}$

Figure 8 – Relative change of exemplary objectives and thrust parameters with BPR and $T_{3,max}$ for $T_{41,TOC} = 1730$ K: The grid data is based on the reference workflow sampling data (N_S = 71), which was used to fit the sensitivity coefficients. The sensitivity-based approximation (coloured surface) is calculated using the estimated sensitivities and the relative changes of engine parameters across the design space according to the reference sampling.

With the thrust parameter sensitivities and the estimated changes, the absolute thrust at TOC and MTO can be calculated based on the given reference values according to equations 12 and 13.

$$\mathrm{FN}_{\mathrm{TOC}} = \mathrm{FN}_{\mathrm{TOC,ref}} \left(1 + \Delta\mathrm{FN}_{\mathrm{TOC}}\right) \tag{12}$$

$$\mathrm{FN}_{\mathrm{MTO}} = \mathrm{FN}_{\mathrm{MTO,ref}} \left(1 + \Delta\mathrm{FN}_{\mathrm{MTO}}\right) \tag{13}$$

The required thrust input values for the evaluation of the rubber engine model and for the operating condition cruise are set according to equations 14 to 16.

$$\mathrm{FN}_{\mathrm{TOC,in}} = \mathrm{FN}_{\mathrm{TOC}} \tag{14}$$

$$\mathrm{FN}^{*}_{\mathrm{MTO,in}} = \frac{\mathrm{FN}_{\mathrm{MTO}}}{\mathrm{FN}_{\mathrm{TOC}}} \tag{15}$$

$$\mathrm{FN}_{\mathrm{CR,in}} = \mathrm{FN}^{*}_{\mathrm{CR,ref}} \left(1 + \Delta\mathrm{FN}^{*}_{\mathrm{CR}}\right) \mathrm{FN}_{\mathrm{TOC,ref}} \tag{16}$$

Figure 8 shows the response surfaces (coloured) resulting from the sensitivity-based approximation for exemplary parameters. A comparison with the observed workflow sampling data (grid data), which was used to fit the sensitivity coefficients, is presented. The approximations reproduce not only the absolute relative changes well but also the local gradients, which are even more important for the subsequent engine model-integrated optimization. Only in the case of the thrust ratio for MTO in figure 8f, the complex topology is not resolved by the approximation model and only the general trend is roughly captured.

Table 2 – Overview of calculated non-dimensional sensitivities with ∂M_j (columns) and ∂p_i (rows). The shown coefficient values are only valid for the considered long-range aircraft configuration and the specifics of the OAD workflow setup. No generality can be assumed and the application for other use cases has to be critically evaluated.

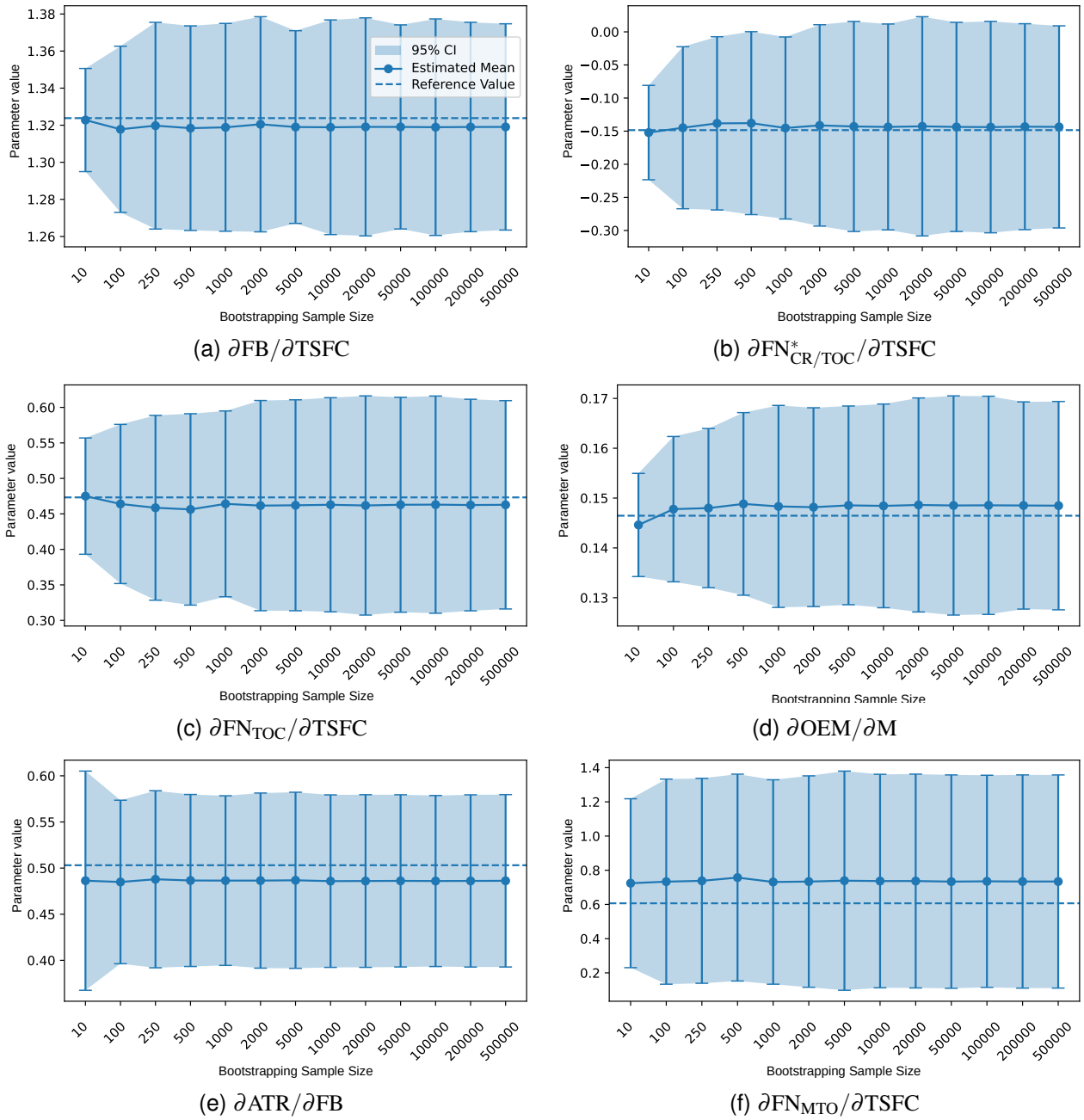
$\partial M_j / \partial p_i$	∂FB	∂OEM	∂ATR	$\partial\mathrm{FN}_{\mathrm{TOC}}$	$\partial\mathrm{FN}^{*}_{\mathrm{CR}}$	$\partial\mathrm{FN}_{\mathrm{MTO}}$
∂TSFC	1.3238	0.1047	-	0.4732	-0.1485	0.6068
∂M	0.1222	0.1465	-	0.1868	-0.0625	-
∂D	0.1259	0.0604	-	0.0742	0.0664	0.4441
∂L	0.0788	0.0384	-	0.0401	0.0332	-
∂EINOx	-	-	0.2144	-	-	-
∂FB	-	-	0.5031	-	-	-
∂H	-	-	-0.2257	-	-	-

3.2 Uncertainty Results

A DoE with a large number of samples $N_{\mathrm{S,ref}} = 71$ and corresponding top-level workflow executions was used to determine the sensitivity coefficients in section 3.1. However, it is aimed for a lower number of samples to reduce the calculation effort and it cannot be assumed that this many points are generally available to determine the sensitivity coefficients of the linearized approximation model. It is relevant to investigate the quality of determined sensitivity coefficients and the associated uncertainty range when lower numbers of samples are used for fitting. Therefore, the set of sensitivity coefficients is determined for various smaller selections N_{S} as subsets of $N_{\mathrm{S,ref}} = 71$. These selections are randomly chosen from the total set multiple times to make a statistical evaluation, a technique known as bootstrapping.

3.2.1 Bootstrapping Sample Size

For a selection of $N_S = 5$ from $N_{S,ref} = 71$, there are over 13 million possible combinations. For $N_S = 7$, there are more than a billion combinations and this number increases even further for larger selections up to $N_S = 35$. A study on the influence of the bootstrapping sample size N_B is carried out first to determine a suitable value of N_B for the uncertainty assessment. Random combinations of $N_S = 7$ points are selected for various N_B (number of selections), and the sensitivity coefficients of the approximation model are calculated for each case. Then, the mean value and 95 % confidence interval (CI) are determined for the analyses based on the standard deviation. Figure 9 exemplary shows the results for selected sensitivity coefficients.



(a) $\partial FB/\partial TSFC$

(b) $\partial FN^*_{CR/TOC}/\partial TSFC$

(c) $\partial FN_{TOC}/\partial TSFC$

(d) $\partial OEM/\partial M$

(e) $\partial ATR/\partial FB$

(f) $\partial FN_{MTO}/\partial TSFC$

Figure 9 – Uncertainty analysis for a sample size of $N_S = 7$ and different bootstrapping sizes N_B (number of subsets with 7 samples randomly selected from $N_{S,ref} = 71$).

Off-sets in the mean value of the determined sensitivity coefficients are observed for all parameters. These shifts are particularly noticeable e.g. for ∂ATR and ∂FN_{MTO} up to very large bootstrapping sample sizes N_B of several hundred thousand points. When the linear regression is made on the basis of only a small subsample of the full dataset, the resulting sensitivity coefficients are highly

variable and strongly influenced by noise and the configuration of the selected points. Even when a large number of subsamples N_{B} is used for regression and the resulting sensitivity coefficients are averaged, the deviation from the regression result obtained for the full dataset with $N_{\mathrm{S,ref}} = 71$ does not vanish. The mean value of the subsample-based estimators $\mathrm{E}[\hat{\beta}_7]$ converges towards the expectation value of the estimator distribution for $N_{\mathrm{S}} = 7$, which is usually different from the solution obtained from regression of all data points $\hat{\beta}_{71}$. The reason is that the ordinary least squares estimator $\hat{\beta}$ is a non-linear function of the sampled data (see Eq. 17) where X is the matrix of independent variables, X^T its transpose and y the vector of dependent observations.

$$\hat{\beta} = (\mathrm{X^T X})^{-1}\mathrm{X^T y} \quad \text{with} \quad \mathrm{E}[\hat{\beta}_7] \neq \hat{\beta}_{71} \tag{17}$$

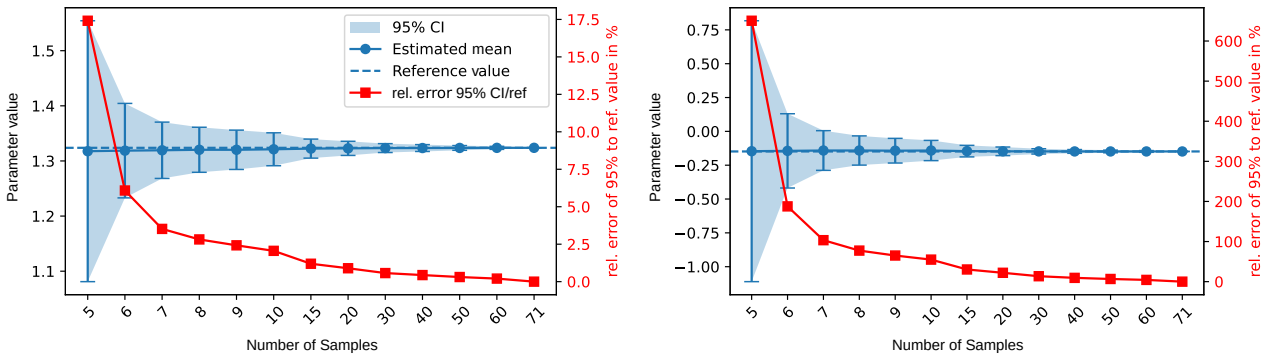
This effect is more pronounced for noisy and/or non-perfectly linear data-relations since small subsamples do not fully capture the underlying structure of the complete dataset allowing individual points to exert disproportionate influence on the regression result. This explanation aligns with the observation that the parameters with the largest scatter in figure 7 also have the largest shift in the mean value in figure 10. Increasing the number of bootstrap subsets only reduces the Monte Carlo variability of the estimated mean and does not address the systematic deviation from the regression solution of the full dataset. Overall, the mean values of the analyses remain almost constant for $N_{\mathrm{B}} \geq 2000$. Also, the limit values of the 95% confidence intervals only change slightly beyond $N_{\mathrm{B}} = 2000$. Therefore, the bootstrapping size $N_{\mathrm{B}} = 2000$ is a good compromise between sufficient convergence and avoiding unnecessary numerical effort during the subsequent uncertainty analyses.

3.2.2 Sample Size for Sensitivity Calculation

A variation of N_{S} is carried out for the selected bootstrapping size $N_{\mathrm{B}} = 2000$ to determine the influence of N_{S} on the sensitivity coefficient values and to investigate how many samples are required to obtain sufficiently accurate sensitivity values.

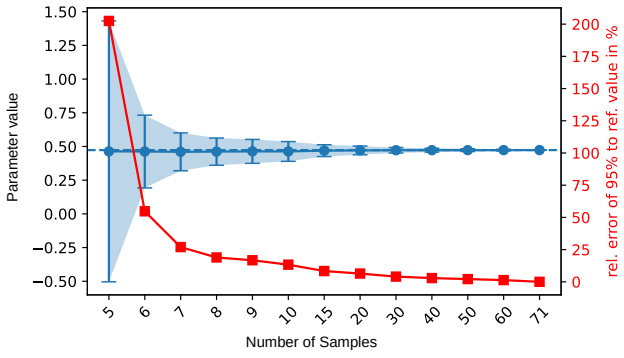
The results for selected sensitivity coefficients are presented in figure 10 and show that the uncertainty range for 95 % CI decreases with increasing N_{S} towards the reference solution with $N_{\mathrm{S,ref}} = 71$. Similar pattern are observed for most parameters. For example, the uncertainty decreases significantly for the sensitivity coefficient $\partial\mathrm{FB}/\partial\mathrm{TSFC}$ when the number of sampling points increases from 5 to 6 as shown in figure 10a. The uncertainty reduces constantly with N_{S} but with a progressively decreasing rate. Another characteristic is found e.g. for the sensitivities $\partial\mathrm{ATR}$ and $\partial\mathrm{FN_{MTO}}$ as illustrated in figures 10e and 10f. For both, there is a significant deviation from the reference mean value at low numbers of N_{S}, which decreases with N_{S} and almost vanishes beyond $N_{\mathrm{S}} \approx 20$. Additionally, the uncertainty band does only shrink slightly at low values of N_{S} and remains relatively high up to large sample sizes N_{S}.

Figure 10 also shows the relative deviation from the reference value of the sensitivity coefficient. This relative error in determining the coefficient has to be expected at a given sample size N_{S} for 95 % CI. The very different magnitude in the relative error is mainly due to the very different absolute values of the coefficients. For larger absolute values, such as $\partial\mathrm{FB}/\partial\mathrm{TSFC}$, the relative error falls quickly below 5 % with increasing N_{S} while the relative error remains very high for small absolute values such as $\partial\mathrm{FN^*_{CR}}/\partial\mathrm{TSFC}$. It shows that no general limit values in terms of relative errors can be introduced to guide the selection of N_{S}. A sample size of N_{S} = 20 is expected to be sufficiently accurate for the considered application case. An elevated level of uncertainty has to be expected for ATR and the thrust at MTO.

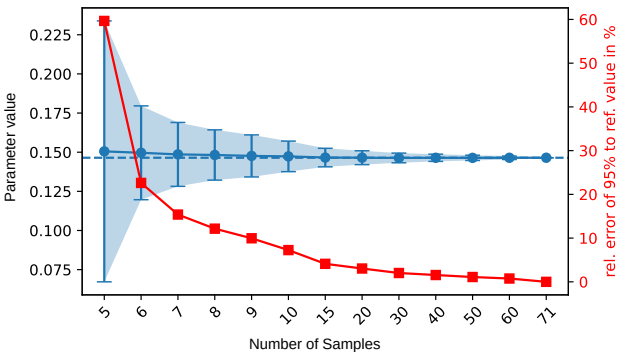


(a) $\partial \mathrm{FB}/\partial \mathrm{TSFC}$

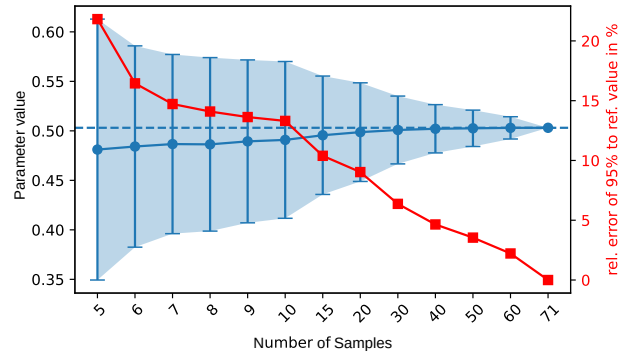
(b) $\partial \mathrm{FN}^{*}_{\mathrm{CR}}/\partial \mathrm{TSFC}$



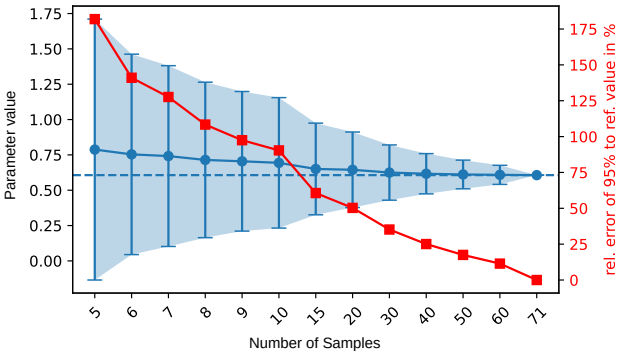
(c) $\partial \mathrm{FN}_{\mathrm{TOC}}/\partial \mathrm{TSFC}$



(d) $\partial \mathrm{OEM}/\partial \mathrm{M}$



(e) $\partial \mathrm{ATR}/\partial \mathrm{FB}$



(f) $\partial \mathrm{FN}_{\mathrm{MTO}}/\partial \mathrm{TSFC}$

Figure 10 – Influence of the variation of p and the resulting confidence intervalls

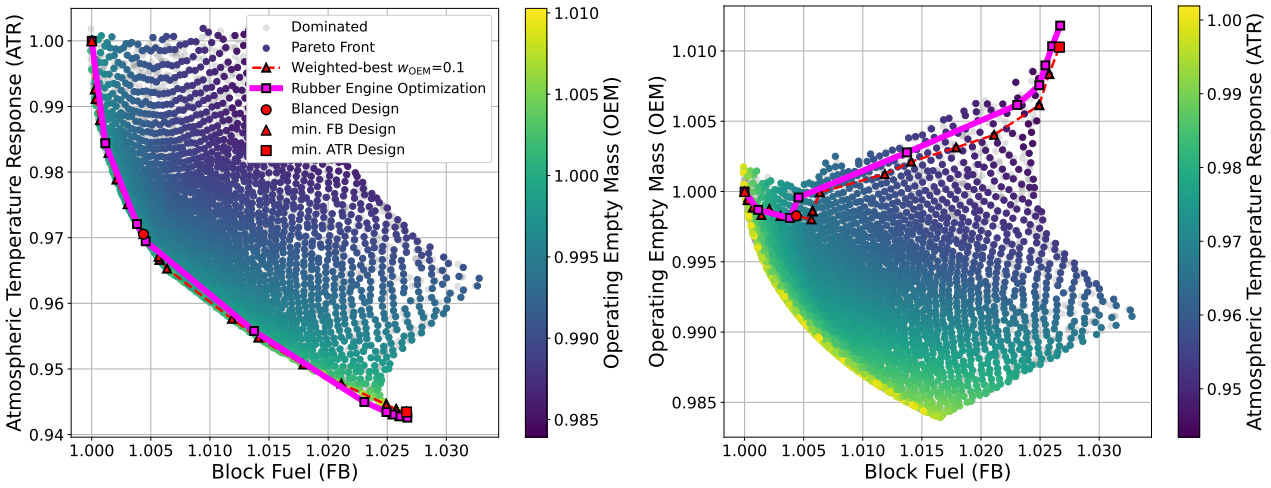
3.3 Optimization Results

The approximated objective function from equation 3 is explicitly written in equation 18 incorporating the approximations of relative changes ΔFB, ΔOEM and ΔATR using the previously calculated sensitivity coefficients with N_S = 71.

$$\min_{\mathbf{x}\in\mathbb{R}^3} \mathbf{f}(\mathbf{x}) = w_{\mathrm{FB}}\,(1+\Delta\mathrm{FB}) + w_{\mathrm{OEM}}\,(1+\Delta\mathrm{OEM}) + w_{\mathrm{ATR}}\,(1+\Delta\mathrm{ATR}) \tag{18}$$

The rubber engine model-integrated optimization strategy described in section 2.4 and as visualized in figures 1 and 5 is applied to optimize ten engines for different combinations of weighting coefficients w_{FB} and w_{ATR} maintaining a constant value for $w_{\mathrm{OEM}} = 0.1$ according to the selected weighted-best line of the reference solution. Figure 11 compares the reference solution with the resulting Pareto-front produced with the rubber engine model-integrated optimization strategy.

The location and shape of the Pareto-front for the weighted-best line ($w_{\mathrm{OEM}} = 0.1$) matches well. Additionally, the selected designs for min. FB and min. ATR as well as the balanced design with



(a) ΔFB-ΔATR-Projection

(b) ΔFB-ΔOEM-Projection

Figure 11 – Pareto-front for the exemplary multi-objective engine optimization problem. The reference solution is compared to the resulting Pareto-front employing the rubber engine model-integrated strategy (magenta line, square markers with black border).

the respective weighting coefficient sets lie closely together on the Pareto-fronts comparing the reference solution with the rubber engine-integrated optimization. The largest deviation occurs for the min. ATR engine design with respect to OEM (see Fig. 11b). Table 3 compares important engine parameters for the three designs showing relative deviations between the solutions found with the different optimization approaches.

Table 3 – Comparison between selected points of the reference Pareto-front and the obtained results using the rubber engine model-integrated optimization strategy.

Design	**min. FB Design**			**Balanced Design**			**min. ATR Design**		
	Reference Solution	Model-Integrated Optimization	rel. Dev.	Reference Solution	Optimized Optimization	rel. Dev.	Reference Solution	Model-Integrated Optimized	rel. Dev.
Objectives									
FB/FB_{ref}	1.000	1.000	0.0	1.004	1.004	-0.1	1.027	1.027	0.0
ATR/ATR_{ref}	1.000	1.000	0.0	0.971	0.972	0.2	0.943	0.943	-0.1
OEM/OEM_{ref}	1.000	1.000	0.0	0.998	0.998	0.0	1.010	1.012	0.2
Decision Variables									
BPR	12.877	12.452	-3.4	13.147	12.726	-3.3	13.868	13.761	-0.8
$T_{3,max}$	967	964	-0.3	939	937	-0.2	885	878	-0.8
$T_{41,TOC}$	1750	1750	0.0	1750	1750	0.0	1700	1700	0.0
Constraints									
$T_{41,TOC}$	1750	1750	0.0	1750	1750	0.0	1700	1700	0.0
$T_{3,max}$	967	964	-0.3	939	937	-0.2	885	878	-0.8
$T_{41,CR}$	1590	1572	-1.1	1588	1571	-1.1	1541	1523	-1.2
$T_{41,max}$	1826	1829	0.2	1829	1830	0.1	1778	1771	-0.4
$T_{45,max}$	1245	1250	0.4	1270	1274	0.3	1275	1275	0.0
$R_{t,Fan}$	1.492	1.463	-2.0	1.486	1.459	-1.9	1.533	1.518	-1.0
h_{HPC}	0.0180	0.0180	0.1	0.0187	0.0187	-0.1	0.0210	0.0210	0.4
N_{HPC}	8	8	0.0	7	7	0.0	7	7	0.0
N_{LPT}	4	4	0.0	4	4	0.0	4	4	0.0
SM_{Fan}	6.248	6.858	8.9	6.438	7.015	8.2	5.535	5.774	4.1

The objectives are predicted very accurately with maximum relative deviations of ≈ 0.2 %. In terms of the decision variables, the temperatures $T_{3,\max}$ and $T_{41,\mathrm{TOC}}$ belonging to the optimal solutions are very close with a maximum difference of 7 K in case of the min. ATR design. However, there are differences for BPR with a maximum relative deviation of 3.4 % for the min FB design. In the optimal region, the change of BPR has only a small impact on the objectives as observed in figures 8a and 8c. Therefore, a small uncertainty in the approximation model will lead to a relatively large deviation in the selected optimal BPR. Most of the constraint parameters are matched well having relative

deviations less than 1 %. Only three parameters show higher deviations: First, the temperature T_{41} at cruise conditions deviates constantly by $\approx$ 1.1-1.2 %. This is caused by different cruise conditions. While the engine model-integrated strategy is evaluated for the typically flown mission, the constraint was calculated for the mid cruise condition of the design mission in case of the reference solution. Since the design mission requires a higher thrust at cruise, the operating temperature is higher for the reference solution. However, the constraint for $T_{41,\mathrm{CR}}$ is not reached and therefore, does not impact the found optima. Second, the fan tip radius $R_{t,\mathrm{FAN}}$ is larger by up to 2 % for the reference solution. This is related to the already discussed effect due to BPR. Third, the fan surge margin deviates by up to $\approx$ 9 % for the found solutions. The surge margin is assessed at the maximum take-off condition. The related thrust approximation for $\mathrm{FN}_{\mathrm{MTO}}$ was found to be highly uncertain in section 3.1 as shown in figure 7e and causes the relative deviation in $\mathrm{SM}_{\mathrm{Fan}}$. However, also the constraint for $\mathrm{SM}_{\mathrm{Fan}}$ is not limiting and does not restrict the selection of optimal solutions in case of the presented study.

4. Discussion

The rubber engine model-integrated optimization strategy employs a sub-level engine optimization with respect to top-level objectives. The objectives are approximated with constant sensitivity coefficients following a superposition approach. The proposed engine model-integrated strategy produces qualitatively and quantitatively similar optimization results as the reference approach using a large DoE in combination with surrogate-based optimization. Relevant uncertainty was mainly observed for the decision variable BPR and constraints that are evaluated at take-off conditions. For the investigated case, the MTO-related constraints were not limiting, but they might be limiting for another application scenario or problem formulation and could cause higher deviations with respect to the optimal solutions. The uncertainty in the approximated thrust $\mathrm{FN}_{\mathrm{MTO}}$ is related to the limited number and quality of identified parameter correlations: The change in $\mathrm{FN}_{\mathrm{MTO}}$ during sub-level optimization is modelled based on TSFC and nacelle diameter only. Further parameters influence the thrust value, which were omitted here since no clear dependency was found and relevant aircraft parameters are not available on engine level.

The rubber engine model evaluation for selecting a design and calculating the cruise operating point is computationally cheap (< 1 s). The rubber engine model-integrated optimization process requires $\approx$ 15-40 s to find the optimal solution for a given set of weighting coefficients. With these computationally cheap executions, the OAD workflow requires approximately the same time $\approx 1-2.5$ h for one converged run. Solving the approximated optimization problem at engine-level and returning an optimized engine in each level-1 iteration step of the OAD workflow (see Fig. 3) solves the entire optimization problem with acceptable uncertainty in only one workflow execution. However, the calculation of sensitivities requires further computational effort if they are not available from the beginning. A reliable calculation of sensitivities requires the sampling size N_S = 20 and a total computational time of $\approx$ 35 h. Therefore, the total time to obtain an optimized result is $\approx$ 1.5 days for the proposed rubber engine model-integrated optimization strategy. The approach has the potential to accelerate the optimization by a factor of 3.5 compared to the reference strategy coming at the cost of introduced uncertainty. However, another advantage of the proposed sub-level optimization is increased flexibility. When the sensitivities are calculated once, small variations induced by other disciplines and the impact on the aircraft configuration can be mapped while continuously optimizing the engine. In contrast, the reference strategy would require a large and computationally expensive DoE each time to achieve this.

5. Conclusions

The proposed rubber engine model-integrated optimization strategy achieved results comparable to a surrogate-based reference optimization while substantially reducing overall computational effort by a factor of 3.5. By combining sub-level engine optimization with top-level sensitivity information, optimized aircraft-engine configurations can be obtained within a single OAD workflow execution. Although the approach introduces some uncertainty, particularly for take-off-related constraints, it offers a favourable trade-off between accuracy, computational efficiency, and flexibility, enabling a faster exploration of design variations and multidisciplinary interactions. Therefore, the method represents a

promising alternative to computationally expensive top-level optimization strategies for early aircraft-engine design studies.
Future work should focus on improving the representation of take-off-related engine characteristics and the identification of further parameter correlations with corresponding sensitivities to reduce the uncertainty in the approximated optimization problem. In addition, the applicability of the proposed strategy should be assessed for other aircraft classes, engine architectures and multidisciplinary optimization problems.

6. Contact Author Email Address

Jannik Häßy
German Aerospace Center (DLR), Institute of Propulsion Technology
Linder Höhe, 51147 Cologne, Germany
mailto: jannik.haessy@dlr.de

7. Copyright Statement

The authors confirm that they, and/or their company or organization, hold copyright on all of the original material included in this paper. The authors also confirm that they have obtained permission, from the copyright holder of any third party material included in this paper, to publish it as part of their paper. The authors confirm that they give permission, or have obtained permission from the copyright holder of this paper, for the publication and distribution of this paper as part of the ICAS proceedings or as individual off-prints from the proceedings.

References

[1] Jannik Häßy. “Hybrid Surrogate-Based Rubber Engine Model for Integration of Aero Engine Conceptual Design into Overall Aircraft Multidisciplinary Design”. Dissertation. Technische Universtität Berlin, Forthcoming.

[2] Jannik Häßy and Benjamin Fröhler. “The Virtual Propulsion Expert: Application of a Hybrid Surrogate-Based Rubber Engine Model in Aircraft Design”. In: *AIAA AVIATION 2023 Forum*. Reston, Virginia: American Institute of Aeronautics and Astronautics, June 12, 2023. ISBN: 978-1-62410-704-7. DOI: 10.2514/6.2023-4304.

[3] Jannik Häßy, Jens Schmeink, Richard Becker, Stanislaus Reitenbach, Maximilian Vieweg, Philipp Bekemeyer, and Andrei Merle. “Hybrid Surrogate-Based Rubber Engine Model for Aircraft Multidisciplinary Design Optimization”. In: *AIAA AVIATION 2020 FORUM*. Reston, Virginia: American Institute of Aeronautics and Astronautics, June 15, 2020. ISBN: 978-1-62410-598-2. DOI: 10.2514/6.2020-3186.

[4] R.-G. Becker, S. Reitenbach, C. Klein, T. Otten, M. Nauroz, and M. Siggel. “An Integrated Method for Propulsion System Conceptual Design”. In: *Proceedings of the ASME Turbo Expo: Turbine Technical Conference and Exposition - 2015*. New York, NY: ASME, 2015. ISBN: 978-0-7918-5662-8. DOI: 10.1115/GT2015-43251.

[5] Stanislaus Reitenbach, Alexander Krumme, Thomas Behrendt, Markus Schnös, Thomas Schmidt, Sandrine Hönig, Robert Mischke, and Erwin Mörland. “Design and Application of a Multidisciplinary Predesign Process for Novel Engine Concepts”. In: *Journal of Engineering for Gas Turbines and Power* 141.1 (2019). ISSN: 0742-4795. DOI: 10.1115/1.4040750.

[6] Stanislaus Reitenbach, Maximilian Vieweg, Richard Becker, Carsten Hollmann, Florian Wolters, Jens Schmeink, Tom Otten, and Martin Siggel. “Collaborative Aircraft Engine Preliminary Design using a Virtual Engine Platform, Part A: Architecture and Methodology”. In: *AIAA Scitech 2020 Forum*. Reston, Virginia: American Institute of Aeronautics and Astronautics, Jan. 6, 2020. ISBN: 978-1-62410-595-1. DOI: 10.2514/6.2020-0867.

[7] Jannik Häßy and Jens Schmeink. “Knowledge-Based Conceptual Design Methods for Geometry and Mass Estimation of Rubber Aero Engines”. In: *ICAS 2022 - 33rd Congress of the International Council of the Aeronautical Sciences*. 2022. URL: https://elib.dlr.de/192376/ (visited on 04/16/2023).

[8] Jannik Häßy, Martin Bolemant, and Richard-Gregor Becker. “An Educated Guess - Predicting Turbomachinery Efficiencies of Aero Engines During Conceptual Design”. In: *Proceedings of ASME Turbo Expo 2023: Turbomachinery Technical Conference and Exposition (GT 2023)*. New York, N.Y.: The American Society of Mechanical Engineers, 2023. ISBN: 978-0-7918-8693-9. DOI: 10.1115/GT2023-103638.

[9] Benjamin Fröhler, Jannik Häßy, and Mohammad Abu-Zurayk. “Development of a Medium/Long-Haul Reference Aircraft”. In: *71. Deutscher Luft- und Raumfahrtkongresses (DLRK) 2022*. Ed. by DGLR. 2022.

[10] D. Seider, P. M. Fischer, M. Litz, A. Schreiber, and A. Gerndt. “Open source software framework for applications in aeronautics and space”. In: *2012 IEEE Aerospace Conference*. Piscataway, NJ: IEEE, 2012, pp. 1–11. ISBN: 978-1-4577-0557-1. DOI: 10.1109/AERO.2012.6187340.

[11] Björn Nagel, Daniel Böhnke, Volker Gollnick, Peter Schmollgruber, Arthur Rizzi, Gianfranco La Rocca, and Juan J. Alonso. “Communication in Aircraft Design: Can we establish a Common Language?” In: *ICAS 2012 - 28nd Congress of the International Council of the Aeronautical Sciences*. Australien, Brisbane, Aug. 20, 2012. URL: http://icas.org/ICAS_ARCHIVE/ICAS2012/PAPERS/201.PDF (visited on 11/15/2022).

[12] Marko Alder, Erwin Moerland, Jonas Jepsen, and Björn Nagel. “Recent Advances in Establishing a Common Language for Aircraft Design with CPACS”. In: *Aerospace Europe Conference 2020*. Ed. by CEAS. Feb. 25, 2020. URL: https://elib.dlr.de/134341/ (visited on 11/15/2022).

[13] Sebastian Wöhler, Georgi Atanasov, Daniel Silberhorn, Benjamin Fröhler, and Thomas Zill. “Preliminary Aircraft Design within a Multidisciplinary and Multifidelity Design Environment”. In: *Aerospace Europe Conference*. 2020. URL: https://elib.dlr.de/185515/.

[14] Emily Schwartz Dallara. “Aircraft design for reduced climate impact”. Ph.D. Thesis. Stanford University, 2011.

[15] Steven G. Johnson. *The NLopt nonlinear-optimization package*. 2007. URL: https://github.com/stevengj/nlopt.

[16] M. J. D. Powell. “A direct search optimization method that models the objective and constraint functions by linear interpolation”. In: *Advances in Optimization and Numerical Analysis*. Ed. by S. Gomez and J.-P. Hennart. Vol. 275. Mathematics and Its Applications. Springer, 1994, pp. 51–67. DOI: 10.1007/978-94-015-8330-5_4.

[17] Philipp Bekemeyer et al. “Data-Driven Aerodynamic Modeling Using the DLR SMARTy Toolbox”. In: *AIAA AVIATION 2022 Forum*. Reston, Virginia: American Institute of Aeronautics and Astronautics, June 27, 2022. ISBN: 978-1-62410-635-4. DOI: 10.2514/6.2022-3899.

[18] Julian Blank and Kalyanmoy Deb. “Pymoo: Multi-Objective Optimization in Python”. In: *IEEE Access* 8 (2020), pp. 89497–89509. DOI: 10.1109/ACCESS.2020.2990567.